

RESEARCH ARTICLE | MAY 03 2007

Artificial fluid properties for large-eddy simulation of compressible turbulent mixing

Andrew W. Cook



Physics of Fluids 19, 055103 (2007)
<https://doi.org/10.1063/1.2728937>



Articles You May Be Interested In

A new subgrid characteristic length for turbulence simulations on anisotropic grids

Physics of Fluids (November 2017)

A numerical study of the wall-modeled large-eddy simulations of attached and separated flows with a semi-coupled synthetic turbulence generator

Physics of Fluids (July 2024)

Numerical investigation of cavitation vortex dynamics in different cavitation patterns coupled implicit large eddy simulation and boundary data immersion method

Physics of Fluids (February 2024)

Artificial fluid properties for large-eddy simulation of compressible turbulent mixing

Andrew W. Cook^{a)}

Lawrence Livermore National Laboratory, Livermore, California 94550

(Received 11 January 2007; accepted 13 March 2007; published online 3 May 2007)

An alternative methodology is described for large-eddy simulation (LES) of flows involving shocks, turbulence, and mixing. In lieu of filtering the governing equations, it is postulated that the large-scale behavior of a LES fluid, i.e., a fluid with artificial properties, will be similar to that of a real fluid, provided the artificial properties obey certain constraints. The artificial properties consist of modifications to the shear viscosity, bulk viscosity, thermal conductivity, and species diffusivity of a fluid. The modified transport coefficients are designed to damp out high wavenumber modes, close to the resolution limit, without corrupting lower modes. Requisite behavior of the artificial properties is discussed and results are shown for a variety of test problems, each designed to exercise different aspects of the models. When combined with a tenth-order compact scheme, the overall method exhibits excellent resolution characteristics for turbulent mixing, while capturing shocks and material interfaces in a crisp fashion. © 2007 American Institute of Physics.

[DOI: [10.1063/1.2728937](https://doi.org/10.1063/1.2728937)]

I. INTRODUCTION

The computational technique of large-eddy simulation (LES) was invented by meteorologists in the 1960s (Refs. 1–3) as a means of representing very high Reynolds number flows on very coarse grids. The method stands in contrast to direct numerical simulation (DNS), where the range of scales is limited to what can be fully represented on the mesh. The standard approach to deriving the LES equations is to apply a low-pass spatial filter to the Navier-Stokes equations in order to remove unresolvable scales of motion. This is typically done without specifying the exact form of the filter function. The LES filter, however, must obey certain constraints, e.g., the transfer function must be identically zero for all wavenumbers above $k_q = \pi/\Delta$, where Δ is the grid spacing. This requirement stems from the fact that the computational grid does not support wavenumbers outside the Nyquist interval. If this requirement is not met, then the spectral content of the discrete variables will be aliased with respect to the filtered variables.⁴ Unfortunately, it is not possible to meet this Fourier-space cutoff with a filter that remains positive-definite in physical space, i.e., any filter satisfying the Nyquist limit will contain negative lobes in real space. This has the unpleasant side effect of generating filtered values outside physical bounds. For example, to ensure that mass fractions remain between zero and one, the real-space filter must strictly reside between zero and one. A more catastrophic potential of nonpositive filters is that they can admit negative densities, which can cause a code to fail when, e.g., velocity is computed from momentum. This situation does not occur in the Reynolds-averaged Navier-Stokes (RANS) approach, because ensemble averages are bounds preserving.

Given that the aliasing and bounds constraints cannot

both be met by a filter of the convolution type, the question then is how to provide an inner-scale cutoff, such that the flow remains smooth with respect to the grid scale. One solution is to integrate the equations between grid points to directly generate a set of second-order finite-difference equations. Such is the approach of implicit large-eddy simulation (ILES).^{5–10} This practice introduces two-dimensional cell-face averages as well as three-dimensional cell-volume averages, which must be related to each other. Typically, this is done implicitly via a numerical reconstruction scheme in one dimension, combined with operator splitting for multidimensional simulations. The truncation error of the numerical scheme can be designed to have desirable dissipative properties for turbulence. Much has been accomplished with ILES and the method appears to be growing in popularity; however, it is restricted to low-order upwind schemes with large dissipation and dispersion errors compared to spectral and compact schemes, which possess superior resolution characteristics for turbulence.^{11–14} Furthermore, since ILES dissipation is typically tied to differences in reconstruction on either side of a cell face, the method can be highly susceptible to grid imprinting.

The objective of this work is to introduce a methodology for LES which allows freedom to choose high-fidelity numerical schemes. Rather than modifying the governing equations or working directly with finite-difference equations, the fluid transport coefficients are altered to provide the sharpest possible cutoff near the Nyquist wavenumber. This work extends previous work on hyperviscosity^{15–17} to include hyperconductivity for contact discontinuities and hyperdiffusivity for material interfaces. At the risk of crowding the LES field with yet another acronym, the method will be referred to as artificial-fluid large-eddy simulation (AFLES). The idea of artificially enlarging the diffusive microscales is not really new; however, the specific models presented herein are new

^{a)}Electronic mail: awcook@llnl.gov

and provide superior performance compared to previous models. The outline of this paper is as follows: In Sec. II the governing equations for compressible turbulent mixing are laid out in strong conservation-law form. In Sec. III, models are presented for the artificial fluid properties. In Sec. IV, the numerical solution technique is outlined. Section V describes results on a variety of test problems and Sec. VI presents conclusions regarding the AFLES methodology.

II. GOVERNING EQUATIONS

Compressible flows comprised of N miscible fluids can be described by the following equations:

$$\frac{\partial \rho Y_i}{\partial t} + \nabla \cdot (\rho Y_i \mathbf{u} + \mathbf{J}_i) = 0, \quad i = 1, 2, \dots, N, \quad (1)$$

$$\frac{\partial \rho \mathbf{u}}{\partial t} + \nabla \cdot [\rho \mathbf{u} \mathbf{u} + p \boldsymbol{\delta} - \boldsymbol{\tau}] = 0, \quad (2)$$

$$\frac{\partial E}{\partial t} + \nabla \cdot [(E + p) \mathbf{u} - \boldsymbol{\tau} \cdot \mathbf{u} + \mathbf{q}] = 0, \quad (3)$$

where ρ is density, Y_i is the mass fraction of species i , $\mathbf{u} \equiv \sum_{i=1}^N Y_i \mathbf{u}_i$ is velocity (with \mathbf{u}_i being species velocity), $\mathbf{J}_i \equiv \rho Y_i (\mathbf{u}_i - \mathbf{u})$ is a diffusive mass flux, p is pressure, $\boldsymbol{\delta}$ is the unit tensor, $\boldsymbol{\tau}$ is the viscous stress tensor, $E \equiv \rho(e + \mathbf{u} \cdot \mathbf{u}/2)$ is total energy (with e being internal energy), and \mathbf{q} is the heat conduction flux. For Newtonian fluids, the viscous stress tensor is

$$\boldsymbol{\tau} = \mu(2\mathbf{S}) + (\beta - \frac{2}{3}\mu)(\nabla \cdot \mathbf{u})\boldsymbol{\delta}, \quad (4)$$

where μ is dynamic (shear) viscosity, β is bulk viscosity, and \mathbf{S} is the symmetric strain rate tensor,

$$\mathbf{S} = \frac{1}{2}[\nabla \mathbf{u} + (\nabla \mathbf{u})^\dagger], \quad (5)$$

where $(\nabla \mathbf{u})^\dagger$ denotes the transpose of the dyadic $\nabla \mathbf{u}$. The conductive heat flux vector is described by Fourier's law,

$$\mathbf{q} = -\kappa \nabla T, \quad (6)$$

where κ is thermal conductivity and T is temperature. The interdiffusion energy flux and the diffusion-thermo (Dufour) energy flux are both neglected in (3). The diffusive mass fluxes can be approximated by

$$\mathbf{J}_i \approx -\rho \left(D_i \nabla Y_i - Y_i \sum_{j=1}^N D_j \nabla Y_j \right), \quad (7)$$

where D_i is a species diffusion coefficient. In this Fickian approximation, pressure and temperature (Soret) forces are neglected and the multicomponent fluid is regarded as a binary mixture of species i and a complementary composite species composed of all other materials.^{18–20} The last term in (7) is included to ensure that $\sum_{i=1}^N \mathbf{J}_i = 0$.

For all but the last test problem to be discussed, the fluids are taken to be ideal gases with the same constant ratio of specific heats. Pressure and temperature are thus computed as

$$p = (\gamma - 1)\rho e, \quad (8)$$

$$T = (\gamma - 1)e/R, \quad (9)$$

where

$$R = R_o \sum_{i=1}^N \frac{Y_i}{M_i} \quad (10)$$

is the apparent gas constant, R_o is the universal gas constant, and M_i is the species molecular weight.

III. ARTIFICIAL FLUID PROPERTIES

Most subgrid-scale (SGS) models for LES are arrived at via physical arguments regarding the effects of unresolved eddies on resolved scales. A critical function of any SGS model or numerical damping scheme is to provide the correct energy transfer rate through the cutoff wavenumber. The models to be presented are based on the idea that artificial viscosity/diffusivity should impart a high-wavenumber bias to the dissipation and therefore approximate the cusp in the Heisenberg-Kraichnan spectral viscosity^{21,22} for isotropic turbulence. The AFLES technique is based on adding grid-dependent components to the transport coefficients appearing in (4), (6), and (7), i.e.,

$$\mu = \mu_f + \mu^*, \quad (11)$$

$$\beta = \beta_f + \beta^*, \quad (12)$$

$$\kappa = \kappa_f + \kappa^*, \quad (13)$$

$$D_i = D_{f,i} + D_i^*, \quad (14)$$

where the f subscripts denote fluid properties and the asterisks denote artificial properties. Like fluid properties, artificial properties are required to be both positive definite and frame invariant. Furthermore, they are required to carry over to the incompressible limit, e.g., viscosity must not depend on sound speed. Unlike fluid properties, artificial properties are designed to vanish in smooth regions while providing strong damping near discontinuities. The following models satisfy all of these requirements:

$$\mu^* = C_\mu \overline{|\nabla^r S|} \Delta^{(r+2)}, \quad (15)$$

$$\beta^* = C_\beta \overline{|\nabla^r S|} \Delta^{(r+2)}, \quad (16)$$

$$\kappa^* = C_\kappa \frac{\rho c_s}{T} \overline{|\nabla^r e|} \Delta^{(r+1)}, \quad (17)$$

$$D_i^* = C_D \overline{|\nabla^r Y_i|} \frac{\Delta^{(r+2)}}{\Delta t} + C_Y \overline{[(Y_i - 1)H(Y_i - 1) - Y_i[1 - H(Y_i)]]} \frac{\Delta^2}{\Delta t}, \quad (18)$$

where $S = (\mathbf{S} : \mathbf{S})^{1/2}$ is the magnitude of the strain rate tensor, $\Delta = (\Delta x \Delta y \Delta z)^{1/3}$ is the local grid spacing, c_s is sound speed, Δt is the time step, and H is the Heaviside function. The polyharmonic operator, ∇^r , denotes a series of Laplacians, e.g., $r=4$ corresponds to the biharmonic operator, $\nabla^4 = \nabla^2 \nabla^2$. This operator imbues the models with k^r wavenumber damp-

ing, similar to a spectral vanishing viscosity.^{23,24} The overbar (\bar{f}) denotes a truncated-Gaussian filter, defined as

$$\bar{f}(\mathbf{x}) = \int_{-L}^L G(|\mathbf{x} - \xi|; L) f(\xi) d^3\xi, \quad (19)$$

where

$$G(\xi; L) = \frac{e^{-6\xi^2/L^2}}{\int_{-L}^L e^{-6\xi^2/L^2} d\xi}, \quad L = 4\Delta. \quad (20)$$

This filter eliminates cusps introduced by the absolute value operator, which in turn, ensures that the artificial transport properties are positive definite. For Cartesian grids, (19) can be applied sequentially along each grid line as

$$\begin{aligned} \bar{f}_j = & \frac{3565}{10368} f_j + \frac{3091}{12960} (f_{j-1} + f_{j+1}) + \frac{1997}{25920} (f_{j-2} + f_{j+2}) \\ & + \frac{149}{12960} (f_{j-3} + f_{j+3}) + \frac{107}{103680} (f_{j-4} + f_{j+4}). \end{aligned} \quad (21)$$

The nondimensional constants appearing in (15)–(18) depend on r (except for C_Y), but do not require adjustment from flow to flow. Setting $r=4$, the following values have been found to work well for a wide variety of test problems: $C_\mu=0.002$, $C_\beta=1$, $C_\kappa=0.01$, $C_D=0.003$ and $C_Y=100$. Except where otherwise noted, these values were used for all of the test problems herein.

The second term in the model for D_i^* has been found very helpful in keeping mass fractions between 0 and 1. It should be mentioned that for (18) to be Galilean invariant, Δt must be chosen independently of \mathbf{u} . This is typically not the case when utilizing the CFL stability criterion. Nevertheless, (18) has been found to be quite useful in practice, since it removes ringing at material interfaces over a minimal number of time steps.

IV. NUMERICAL SOLUTION TECHNIQUE

A. Spatial differencing

For the AFLES method described herein, all first derivatives comprising the gradient and divergence operators in the governing equations are computed according to the tenth-order compact scheme²⁵

$$\begin{aligned} & \beta f'_{j-2} + \alpha f'_{j-1} + f'_j + \alpha f'_{j+1} + \beta f'_{j+2} \\ & = a \frac{f_{j+1} - f_{j-1}}{2\Delta} + b \frac{f_{j+2} - f_{j-2}}{4\Delta} + c \frac{f_{j+3} - f_{j-3}}{6\Delta}, \end{aligned} \quad (22)$$

where f'_j represents the derivative of f at node j , Δ is the spacing between nodes, and

$$\alpha = \frac{1}{2}, \quad \beta = \frac{1}{20}, \quad a = \frac{17}{12}, \quad b = \frac{101}{150}, \quad c = \frac{1}{100}.$$

Similarly, all second derivatives (f''_j), comprising the polyharmonic operators in the artificial fluid properties, are computed according to the tenth-order compact scheme

$$\begin{aligned} & \beta f''_{j-2} + \alpha f''_{j-1} + f''_j + \alpha f''_{j+1} + \beta f''_{j+2} \\ & = a \frac{f_{j+1} - 2f_j + f_{j-1}}{\Delta^2} + b \frac{f_{j+2} - 2f_j + f_{j-2}}{4\Delta^2} \\ & \quad + c \frac{f_{j+3} - 2f_j + f_{j-3}}{9\Delta^2}, \end{aligned} \quad (23)$$

where

$$\alpha = \frac{334}{899}, \quad \beta = \frac{43}{1798}, \quad a = \frac{1065}{1798}, \quad b = \frac{1038}{899}, \quad c = \frac{79}{1798}.$$

B. Temporal integration

The governing equations are advanced in time by casting them all in the form $\dot{\Phi}=F$ and integrating via a five-step fourth-order Runge-Kutta (RK4) method.²⁶ The scheme is

$$\begin{aligned} Q^\eta &= \Delta t F^{\eta-1} + A^\eta Q^{\eta-1} & \eta = 1, \dots, 5 \\ \Phi^\eta &= \Phi^{\eta-1} + B^\eta Q^\eta \end{aligned} \quad (24)$$

where Δt is the time step, η is the RK4 subcycle, and A^η and B^η are

$$\begin{aligned} A^1 &= 0, \\ A^2 &= -6234157559845/12983515589748, \\ A^3 &= -6194124222391/4410992767914, \\ A^4 &= -31623096876824/15682348800105, \\ A^5 &= -12251185447671/11596622555746, \\ B^1 &= 494393426753/4806282396855, \\ B^2 &= 4047970641027/5463924506627, \\ B^3 &= 9795748752853/13190207949281, \\ B^4 &= 4009051133189/8539092990294, \\ B^5 &= 1348533437543/7166442652324. \end{aligned}$$

The fraction of Δt for which the solution advances after each substep is

$$\eta = 1 \Rightarrow 494393426753/4806282396855,$$

$$\eta = 2 \Rightarrow 4702696611523/9636871101405,$$

$$\eta = 3 \Rightarrow 3614488396635/5249666457482,$$

$$\eta = 4 \Rightarrow 9766892798963/10823461281321,$$

$$\eta = 5 \Rightarrow 1.$$

This particular RK4 scheme was chosen for its broad stability properties for both convective and viscous terms. Partial dealiasing is accomplished by applying an eighth-order compact filter to the conserved variables ρY_i , $\rho \mathbf{u}$, and E after each RK4 substep. The compact filter is designed to remove

the top 1/10 of the wavenumbers in as sharp a manner as possible, such that results remain independent of the frequency of filter application (which depends on Δt). The filter stencil is

$$\begin{aligned} & \beta \hat{f}_{j-2} + \alpha \hat{f}_{j-1} + \hat{f}_j + \alpha \hat{f}_{j+1} + \beta \hat{f}_{j+2} \\ &= af_j + \frac{b}{2}(f_{j-1} + f_{j+1}) + \frac{c}{2}(f_{j-2} + f_{j+2}) + \frac{d}{2}(f_{j-3} + f_{j+3}) \\ &+ \frac{e}{2}(f_{j-4} + f_{j+4}), \end{aligned} \quad (25)$$

where \hat{f}_j is the filtered variable and

$$\alpha = 0.66624, \quad \beta = 0.16688, \quad a = 0.99965, \quad \frac{b}{2} = 0.66652, \quad (26)$$

$$\frac{c}{2} = 0.16674, \quad \frac{d}{2} = 4 \times 10^{-5}, \quad \frac{e}{2} = -5 \times 10^{-6}. \quad (27)$$

This compact filter helps prevent the artificial fluid properties from becoming too large. For example, without this filter, β^* can become extremely large in the vicinity of strong shocks, thus driving the viscously stable time step to zero and bringing the simulation to a halt.

C. Stability

The maximum stable time step is limited not only by the inviscid CFL condition,²⁷

$$\Delta t_{\text{CFL}} = \text{MIN}\left(\frac{|u|}{\Delta x} + \frac{|v|}{\Delta y} + \frac{|w|}{\Delta z} + c_s \sqrt{\frac{1}{\Delta x^2} + \frac{1}{\Delta y^2} + \frac{1}{\Delta z^2}}\right)^{-1}, \quad (28)$$

where $(u, v, w) = \mathbf{u}$, but also by the maximum viscosity, conductivity, and diffusivity existing in the domain. Time scales associated with μ , β , κ , and D_i are

$$\Delta t_\mu = \text{MIN}\left(\frac{\rho \Delta^2}{\mu}\right), \quad (29)$$

$$\Delta t_\beta = \text{MIN}\left(\frac{\rho \Delta^2}{\beta}\right), \quad (30)$$

$$\Delta t_\kappa = \text{MIN}\left(\frac{\rho c_s^2 \Delta^2}{\kappa T}\right), \quad (31)$$

$$\Delta t_D = \text{MIN}\left(\frac{\Delta^2}{D_i}\right). \quad (32)$$

The simulation time step is chosen to be

$$\Delta t = \text{MIN}(\Delta t_{\text{CFL}}, 0.2\Delta t_\mu, 0.2\Delta t_\beta, 0.2\Delta t_\kappa, 0.2\Delta t_D). \quad (33)$$

V. RESULTS

The test problems in this section were selected to assess the efficacy of μ^* , β^* , κ^* , and D_i^* for capturing turbulent mixing with shocks and other discontinuities. All problems

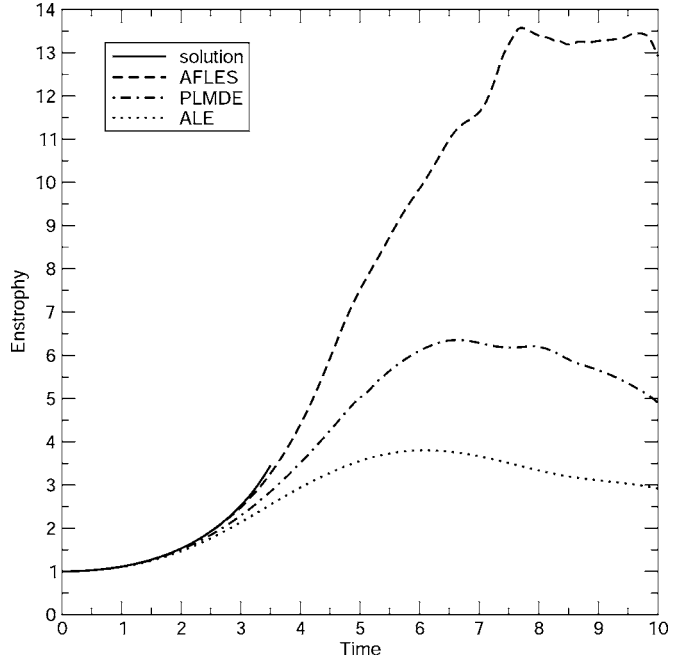


FIG. 1. Normalized enstrophy versus time for the Taylor-Green vortex. Simulations were conducted in a $2\pi^3$ periodic box using 64^3 grid points.

were run in exactly the same manner, using the default values of the model coefficients and setting $\mu_f = \beta_f = \kappa_f = D_{f,i} = 0$. All problem specifications are in nondimensional units.

A. Taylor-Green vortex

The ability of μ^* to accurately capture the evolution of the energy spectrum in high-Reynolds-number decaying turbulence has been previously demonstrated.¹⁶ In that work, C_μ was determined by requiring the viscosity model to provide the correct energy transfer rate for the turbulent cascade. As a further test of the ability of μ^* to resolve small-scale turbulence, we consider here the Taylor-Green vortex.²⁸ The initial conditions are

$$\begin{aligned} \rho &= 1, & u &= \sin(x)\cos(y)\cos(z), \\ v &= -\cos(x)\sin(y)\cos(z), & w &= 0, \\ p &= 100 + \{[\cos(2z) + 2][\cos(2x) + \cos(2y)] - 2\}/16, \end{aligned} \quad (34)$$

$$\gamma = 5/3,$$

where the pressure corresponds to the incompressible flow solution. The arbitrary constant of 100 is selected to make the Mach number very low, such that the incompressible solution can be used for comparison. As the flow evolves, the vortex stretches and bends, thus broadening the spectrum to include higher wavenumbers. Stretching and bending of vortex lines constitute key energy cascade mechanisms in turbulent flows. The computational domain is a triply periodic $(2\pi)^3$ box on a 64^3 grid. Figure 1 shows normalized total enstrophy, i.e., $\Omega(t)/\Omega(0)$, where

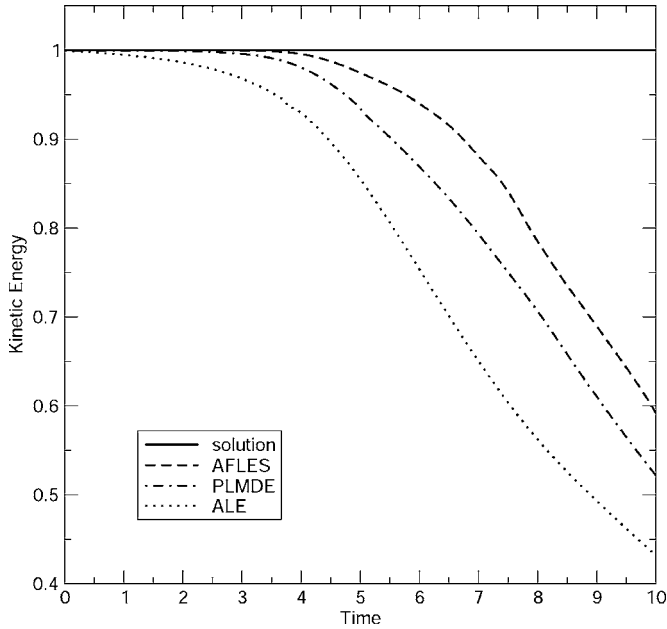


FIG. 2. Normalized kinetic energy versus time for the Taylor-Green vortex.

$$\Omega(t) = \frac{1}{2} \int_V \boldsymbol{\omega} \cdot \boldsymbol{\omega} dV, \quad \boldsymbol{\omega} = \nabla \times \mathbf{u}.$$

Two ILES schemes are included for comparison: a piecewise linear MUSCLE direct Eulerian (PLMDE) scheme²⁹ and an arbitrary Lagrangian Eulerian (ALE) method.³⁰ The theoretical result,³¹ accurate up to about $t=3.5$, is plotted in order to assess the ability of each method to resolve small-scale vortex dynamics. Analysis based on Padé approximants and the behavior of the analyticity strip, predicts $\Omega(t)$ will become far too large to capture on a such a coarse grid;³² nevertheless, the ability of a scheme to track the enstrophy curve, as well as the maximum enstrophy that a scheme is able to generate, provide stringent tests of resolving power. The AFLES method is seen to have much better resolution characteristics than either of the ILES methods.

As a second point of comparison, we examine the evolution of kinetic energy, i.e., $K(t)/K(0)$, where

$$K(t) = \frac{1}{2} \int_V \rho \mathbf{u} \cdot \mathbf{u} dV.$$

This is plotted in Fig. 2, where the AFLES method is seen to better preserve total kinetic energy. The drop-off in energy, beginning at about $t=4$, results from transfer to unresolved wavenumbers. Energy cascading to scales below 2Δ must be removed to prevent it from piling up near the Nyquist limit. If the energy is not removed, then the solution turns to hash, i.e., strong point-to-point oscillations propagate throughout the domain and the spectrum approaches a k^2 power law. This is not the case for the AFLES scheme, as illustrated in Fig. 3, where the spectrum of turbulent kinetic energy is plotted at four different times. Initially, all of the energy resides at the bottom wavenumber. At $t=2$ some of the energy has moved into higher wavenumbers but the flow is still completely resolved (as evidenced by the steep drop-off at

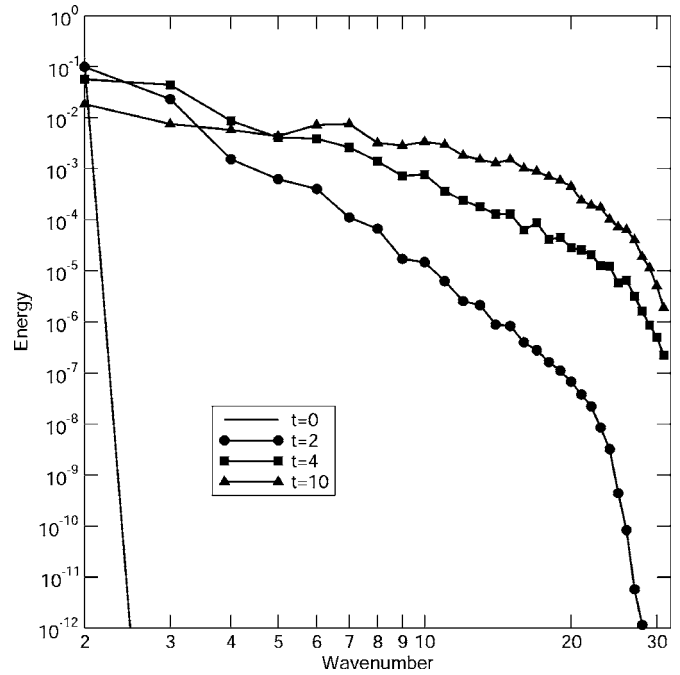


FIG. 3. Evolution of kinetic energy spectrum for the Taylor-Green vortex.

the high end of the spectrum). By $t=4$ the flow is still well resolved. However, energy is beginning to migrate outside the supported band of wavenumbers. By $t=10$ much energy has leaked beneath the grid scale; however, the spectrum has neither curled up nor begun to exhibit a “bottleneck” effect, indicating that ringing in the solution is negligible.

B. Sedov blast wave

In previous studies, the model for β^* was demonstrated to provide $\mathcal{O}(r)$ convergence for smooth flow¹⁵ and capture shocks in approximately three grid points, regardless of shock strength.¹⁷ In order to assess the ability of β^* to capture shocks in a sharp and monotonic fashion in multiple dimensions, we consider the Sedov-Taylor-von Neumann blast wave.³³⁻³⁵ The initial conditions are

$$\rho = 1, \quad \mathbf{u} = 0,$$

$$e = 0.1528415451 \exp(-R^2/\epsilon^2)/\epsilon^3, \quad \epsilon = 0.04, \quad \gamma = 1.4,$$

where $R = \sqrt{x^2 + y^2 + z^2}$ is the radius. The exponential is employed to approximate a delta function on a discrete mesh. The computational domain consists of a uniform Cartesian mesh centered about the origin. Simulations were carried out at two resolutions, using a 128^3 grid ($\Delta = 0.02$) and a 256^3 grid ($\Delta = 0.01$). The results for the density field are displayed in Fig. 4, where the scheme is seen converging to the correct solution. A challenging aspect of this problem is that the blast wave leaves behind a vacuum at the origin. Nevertheless, the AFLES method captures the shock in a crisp angle-independent fashion. Furthermore, integration over the box shows mass, momentum, and total energy to be conserved to more than eight digits.

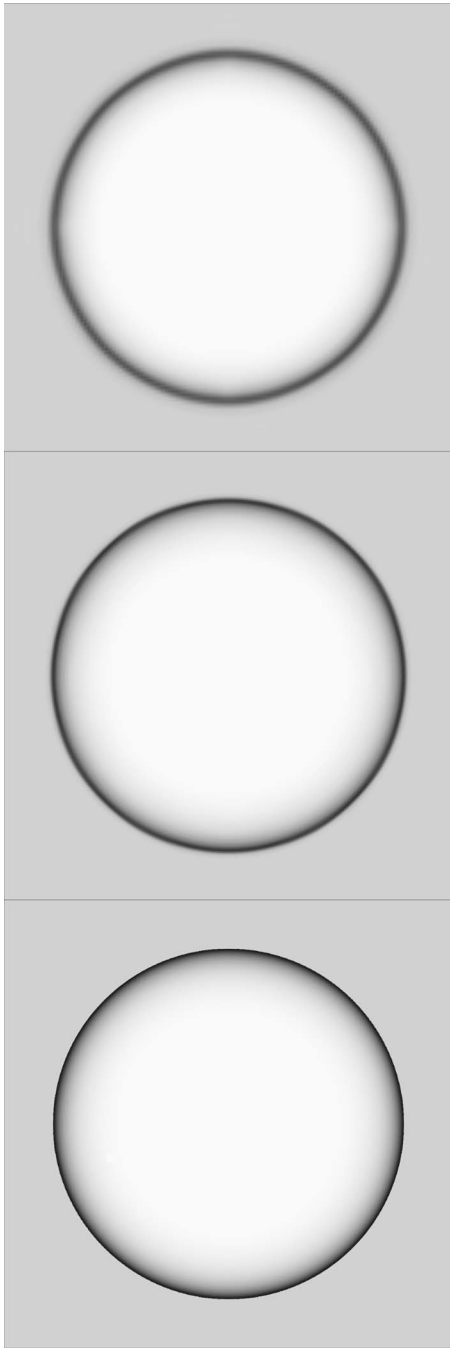


FIG. 4. Density on the $z=0$ plane for the Sedov-Taylor-von Neumann blast wave at $t=1$. White corresponds to $\rho=0$, whereas black corresponds to $\rho=6$. The top image is AFLES with $\Delta=0.02$, the middle image is AFLES with $\Delta=0.01$, and the bottom image is the solution.

C. Contact discontinuities

The need to treat temperature discontinuities independently of shocks was pointed out by Fiorina and Lele.¹⁷ Initial conditions, radiation effects, and chemical reactions are all capable of producing steep temperature gradients in a smoothly varying velocity field. In order to assess the ability of κ^* to capture such gradients, we consider a quiescent fluid containing a jump in entropy. The initial conditions are

$$\rho = 0.1 + 0.9H(x), \quad \mathbf{u} = 0,$$

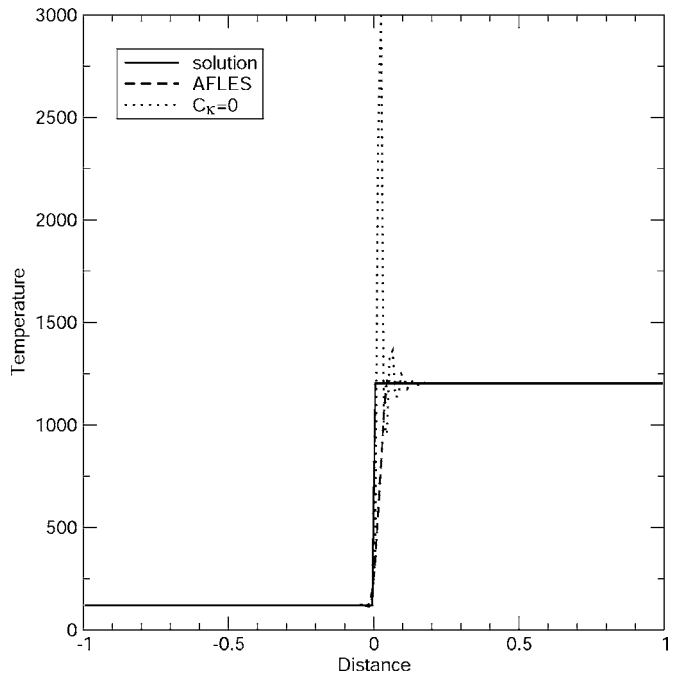


FIG. 5. Temperature at $t=1 \times 10^{-5}$ for the quiescent contact discontinuity using a grid resolution of $\Delta=0.01$.

$$p = 1 \times 10^{10}, \quad \gamma = 5/3.$$

For a nonconducting fluid, this one-dimensional flow should remain fixed at its initial state. Figure 5 shows results of the AFLES method with and without the thermal conductivity model. Without the model ($C_\kappa=0$), Gibbs oscillations, introduced by the compact difference and filter stencils, remain undamped. By including the model, the oscillations are removed and the discontinuity is spread over four to five grid

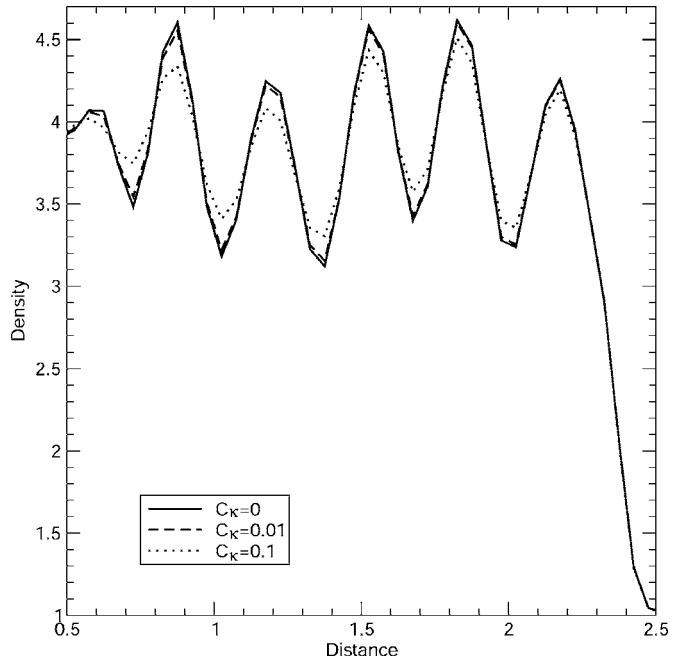


FIG. 6. Density field for the Shu-Osher problem at $t=1.8$ using a grid spacing of $\Delta=0.05$.

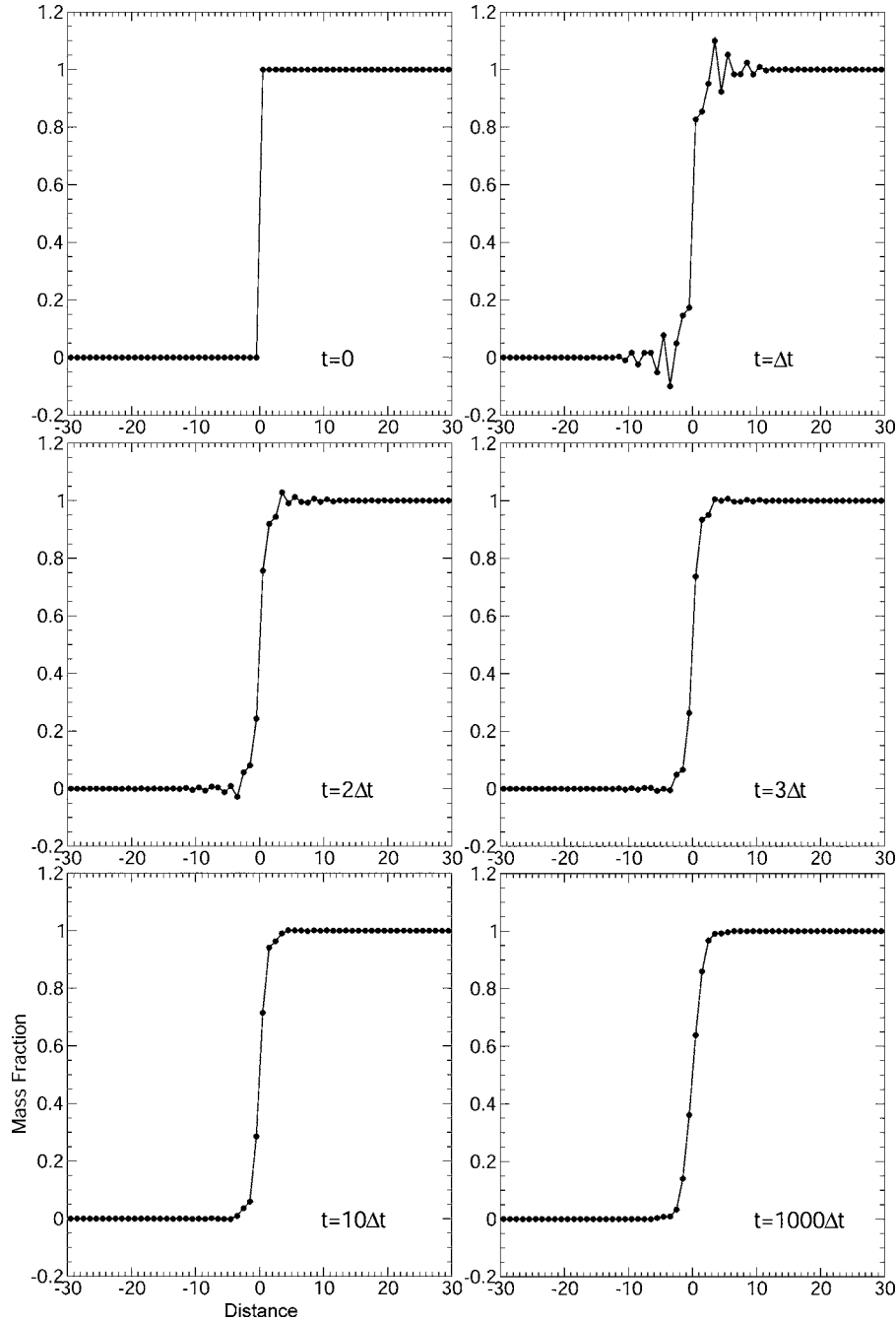


FIG. 7. Evolution of material interface for two adjacent fluids.

points. Once the discontinuity has been sufficiently smoothed, the model essentially turns off, preventing further spreading.

Given that κ^* is necessary for treating jumps in temperature (which remain unaffected by μ^* and β^*), the question arises as to how to determine an upper bound on C_κ to ensure that the model is not excessively dissipative. To answer this question, we turn to the one-dimensional Shu-Osher problem.³⁶ The initial conditions are

$$\rho = 3.857143, \quad p = 10.33333, \quad u = 2.629369 \quad \text{for } x < -4,$$

$$\rho = 1 + 0.2 \sin(5x), \quad p = 1, \quad u = 0 \quad \text{for } x \geq -4, \quad \gamma = 1.4.$$

As the shock propagates into the sinusoidal density field, it leaves a steeply undulating flow in the postshock region. The

postshock undulations are extremely sensitive to thermal conduction, as demonstrated in Fig. 6, which shows AFLES results for three different values of C_κ . With the default value of $C_\kappa=0.01$, the postshock solution remain nearly identical to the case with no artificial thermal conductivity ($C_\kappa=0$). Increasing C_κ to 0.1 however, causes noticeable damping of the undulations.

D. Material interfaces

For flows involving more than one fluid, artificial diffusivity is necessary to avoid ringing in the mass fractions. In order to assess the ability of D_i^* to capture material interfaces, we first consider the simple case of two adjacent fluids in thermodynamic equilibrium. The initial conditions are

$$\rho = 1, \quad \mathbf{u} = 0, \quad p = 1 \times 10^{10},$$

$$Y_1 = H(x), \quad Y_2 = 1 - Y_1, \quad \gamma = 5/3.$$

For immiscible fluids, this one-dimensional problem should remain fixed at its initial state. Numerically, the compact stencils generate Gibbs oscillations about the step function, which are strongly damped within the first few time steps. This process is illustrated in Fig. 7, which displays Y_1 versus x at $t=0, \Delta t, 2\Delta t, 3\Delta t, 10\Delta t$ and $1000\Delta t$. The diffusivity model eliminates virtually all ringing within the first three time steps and then effectively turns off, leaving the interface nearly frozen, as evidenced by the profile after a thousand steps. This behavior is independent of the grid spacing and the size of the time step. The artificial diffusivity spreads interfaces over about four grid points within three or four time steps and then vanishes to prevent further spreading. Despite the initial ringing, the mass of each species is conserved and $\sum_{i=1}^N Y_i = 1$ is satisfied to machine precision at every time step, regardless of proximity to the discontinuity.

In order to test the diffusivity model in the presence of strain, we consider the deformation of a circular blob of material in a time-reversing vortex. Following Leveque³⁷ and Rider and Kothe³⁸ the velocity field is prescribed for all time as

$$u = -\sin^2(\pi x)\sin(2\pi y)\cos(\pi t/t_p),$$

$$v = \sin^2(\pi y)\sin(2\pi x)\cos(\pi t/t_p), \quad t_p = 4,$$

with the blob of material initialized as

$$Y_1 = \{1 + \text{erf}[(\mathcal{R} - 0.15)/\epsilon]\}/2,$$

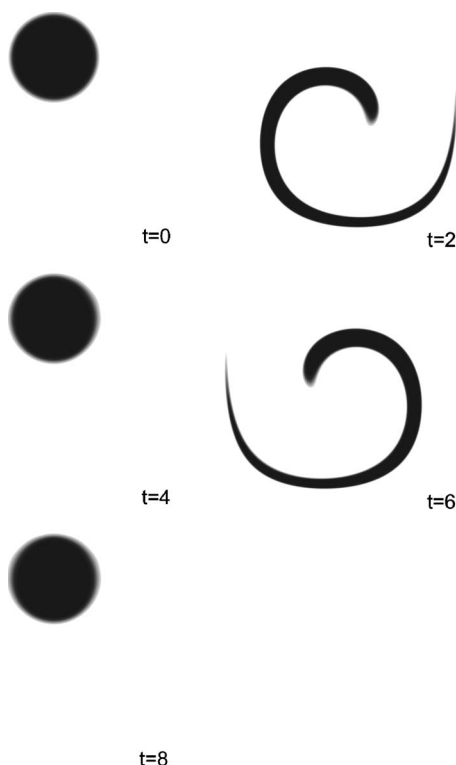


FIG. 8. Scalar advection in a time-reversing vortex.

$$\mathcal{R} = [(x - 0.5)^2 + (y - 0.75)^2]^{1/2}, \quad \epsilon = 0.01.$$

The ϵ parameter imparts a thickness to the material interface to avoid initial ringing. This temporally periodic flow stretches the circular blob into a spiral, then returns to its initial conditions whenever t reaches integer multiples of t_p . This process is depicted in Fig. 8, which shows the blob repeatedly spiraling inward, then returning to its initial state. The straining action causes the interface to thin down to about three or four grid points, at which point the artificial diffusivity turns on to prevent further thinning (which would generate ringing). The amount of mixed fluid produced through artificial diffusion depends on ϵ , t_p , and Δ ; however, for any given set of these parameters, the model becomes active only where necessary to prevent spurious oscillations in the mass fractions.

VI. CONCLUSIONS

Spectral-like models have been introduced for the shear viscosity, bulk viscosity, thermal conductivity, and species diffusivity of an artificial, “LES,” fluid. The models impart a high wavenumber, k' , weighting to the numerical dissipation, thus preserving fidelity at resolved wavenumbers. The models act like switches, turning on only where fields are insufficiently smooth with respect to the grid scale. When the models are combined with high-wavenumber-preserving schemes, a dealiasing filter is required to meet stability constraints and help localize the numerical dissipation. The stencils for the filters and derivative operators in the AFLES scheme are all purely centered; hence, the method is minimally dissipative. The models apply to the incompressible limit without modification and have been successfully used for LES of Rayleigh-Taylor instability.³⁹

The AFLES scheme outperforms standard ILES methods in resolving the enstrophy field of the Taylor-Green vortex. By including the bulk viscosity term in the governing equations, the scheme is able to capture shocks without excessive damping of vorticity. Artificial thermal conductivity helps remove ringing at the heat fronts, while artificial diffusivity helps keep mass fractions within bounds. The five empirical coefficients appearing in the models have been found to exhibit fairly universal behavior, i.e., they appear to work for a wide variety of flows without adjustment. The AFLES method provides a simple and effective approach to LES when the Reynolds number, Mach number, Prandtl number, and/or Schmidt number of a flow is beyond the reach of DNS.

ACKNOWLEDGMENTS

The author is grateful to Dr. W. H. Cabot for help with writing the code. This work was performed under the auspices of the U.S. Department of Energy by the University of California Lawrence Livermore National Laboratory under Contract No. W-7405-Eng-48.

¹J. Smagorinsky, “General circulation experiments with the primitive equations part I: The basic experiment,” Mon. Weather Rev. **91**, 99 (1963).

²D. K. Lilly, “The representation of small-scale turbulence in numerical simulation experiments,” in Proceedings of the IBM Science and Comput-

- ing Symposium on Environmental Science, IBM Data Processing Division (1967), pp. 195–210.
- ³J. W. Deardorff, “A numerical study of three-dimensional turbulent channel flow at large Reynolds numbers,” *J. Fluid Mech.* **41**, 453 (1970).
- ⁴C. E. Shannon, “Communication in the presence of noise,” *Proc. IRE* **37**, 10 (1949).
- ⁵U. Schumann, “Subgrid-scale model for finite-difference simulations of turbulence in plane channels and annuli,” *J. Comput. Phys.* **18**, 376 (1975).
- ⁶V. H. Ransom and J. D. Ramshaw, *Discrete Modeling Considerations in Multiphase Fluid Dynamics* (CRC, Boca Raton, 1992), pp. 3–25.
- ⁷C. Fureby and F. F. Grinstein, “Large eddy simulation of high-Reynolds-number free and wall-bounded flows,” *J. Comput. Phys.* **181**, 68 (2002).
- ⁸L. G. Margolin and W. J. Rider, “A rationale for implicit turbulence modeling,” *Int. J. Numer. Methods Fluids* **39**, 821 (2002).
- ⁹L. G. Margolin and W. J. Rider, “The design and construction of implicit LES models,” *Int. J. Numer. Methods Fluids* **47**, 1173 (2005).
- ¹⁰S. Hickel, N. A. Adams, and J. A. Domaradzki, “An adaptive local deconvolution method for implicit LES,” *J. Comput. Phys.* **213**, 413 (2006).
- ¹¹S. A. Orszag and G. S. Patterson, “Numerical simulation of three-dimensional homogeneous isotropic turbulence,” *Phys. Rev. Lett.* **28**, 76 (1972).
- ¹²D. Gottlieb and S. A. Orszag, *Numerical Analysis of Spectral Methods* (Capital City, Montpelier, 1977).
- ¹³S. Ghosal, “An analysis of numerical errors in large eddy simulations of turbulence,” Annual Research Briefs, Center for Turbulence Research, Stanford University, 1995.
- ¹⁴A. G. Kravchenko and P. Moin, “On the effect of numerical errors in large eddy simulations of turbulent flows,” *J. Comput. Phys.* **131**, 310 (1997).
- ¹⁵A. W. Cook and W. H. Cabot, “A high-wavenumber viscosity for high-resolution numerical methods,” *J. Comput. Phys.* **195**, 594 (2004).
- ¹⁶A. W. Cook and W. H. Cabot, “Hyperviscosity for shock-turbulence interactions,” *J. Comput. Phys.* **203**, 379 (2005).
- ¹⁷B. Fiorina and S. K. Lele, “An artificial nonlinear diffusivity method for supersonic reacting flows with shocks,” *J. Comput. Phys.* **222**, 246 (2007).
- ¹⁸J. O. Hirschfelder, C. F. Curtiss, and R. B. Bird, *Molecular Theory of Gases and Liquids* (Wiley, New York, 1954).
- ¹⁹R. B. Bird, W. E. Stewart, and E. N. Lightfoot, *Transport Phenomena* (Wiley, New York, 1960).
- ²⁰F. A. Williams, *Combustion Theory*, 2nd ed. (Addison-Wesley, Reading, 1985).
- ²¹W. Heisenberg, “Zur statistischen theorie der turbulenz,” *Z. Phys.* **124**, 628 (1948).
- ²²R. H. Kraichnan, “Eddy viscosity in two and three dimensions,” *J. Atmos. Sci.* **33**, 1521 (1976).
- ²³E. Tadmor, “Convergence of spectral methods for nonlinear conservation laws,” SIAM (Soc. Ind. Appl. Math.) *J. Numer. Anal.* **26**, 30 (1989).
- ²⁴G.-S. Karamanos and G. E. Karniadakis, “A spectral vanishing viscosity method for large-eddy simulations,” *J. Comput. Phys.* **163**, 22 (2000).
- ²⁵S. K. Lele, “Compact finite difference schemes with spectral-like resolution,” *J. Comput. Phys.* **103**, 16 (1992).
- ²⁶C. A. Kennedy, M. H. Carpenter, and R. M. Lewis, “Low-storage, explicit Runge-Kutta schemes for the compressible Navier-Stokes equations,” *Appl. Numer. Math.* **35**, 177 (2000).
- ²⁷D. A. Anderson, J. C. Tannehill, and R. H. Pletcher, *Computational Fluid Mechanics and Heat Transfer* (Hemisphere, New York, 1984).
- ²⁸G. I. Taylor and A. E. Green, “Mechanism of the production of small eddies from large ones,” *Proc. R. Soc. London, Ser. A* **158**, 499 (1937).
- ²⁹P. Colella, “A direct Eulerian MUSCL scheme for gas dynamics,” SIAM (Soc. Ind. Appl. Math.) *J. Sci. Stat. Comput.* **6**, 104 (1985).
- ³⁰M. M. Marinak, G. D. Kerbel, N. A. Gentile, O. Jones, D. Munro, S. Pollaine, T. R. Dittrich, and S. W. Haan, “Three-dimensional HYDRA simulations of National Ignition Facility targets,” *Phys. Plasmas* **8**, 2275 (2001).
- ³¹M. E. Brachet, D. I. Meiron, S. A. Orszag, B. G. Nickel, R. H. Morf, and U. Frisch, “Small-scale structure of the Taylor-Green vortex,” *J. Fluid Mech.* **130**, 411 (1983).
- ³²R. H. Morf, S. A. Orszag, and U. Frisch, “Spontaneous singularity in three-dimensional, inviscid, incompressible flow,” *Phys. Rev. Lett.* **44**, 572 (1980).
- ³³L. I. Sedov, *Similarity and Dimensional Methods in Mechanics*, 4th ed. (Academic, New York, 1959).
- ³⁴G. I. Taylor, “The formation of a blast wave by a very intense explosion: I,” *Proc. R. Soc. London, Ser. A* **201**, 155 (1950).
- ³⁵L. D. Landau and E. M. Lifshitz, *Fluid Mechanics* (Addison-Wesley, Reading, 1959).
- ³⁶C.-W. Shu and S. J. Osher, “Efficient implementation of essentially nonoscillatory shock capturing schemes II,” *J. Comput. Phys.* **83**, 32 (1989).
- ³⁷R. J. Leveque, “High-resolution conservative algorithms for advection in incompressible flow,” SIAM (Soc. Ind. Appl. Math.) *J. Numer. Anal.* **33**, 627 (1996).
- ³⁸W. J. Rider and D. B. Kothe, “Reconstructing volume tracking,” *J. Comput. Phys.* **141**, 112 (1998).
- ³⁹A. W. Cook, W. Cabot, and P. L. Miller, “The mixing transition in Rayleigh-Taylor instability,” *J. Fluid Mech.* **511**, 333 (2004).